

Article

Nano-Alloy FeSb Wrapped in Three-Dimensional Honeycomb Carbon for High-Performance Lithium-Ion Batteries

Nanjun Jia ¹, Xinming Nie ¹, Jianwei Li ^{1,*} and Wei Qin ^{2,*} 

¹ School of Physics and Electronic Engineering, Jiangsu Normal University, Xuzhou 221116, China; jnjsnu@163.com (N.J.); nxinming@jsnu.edu.cn (X.N.)

² College of Materials Science and Engineering, Changsha University of Science and Technology, Changsha 410114, China

* Correspondence: jwl189@jsnu.edu.cn (J.L.); qinwei@csust.edu.cn (W.Q.)

Abstract

Sb-based anodes have great potential in lithium-ion batteries because of their relatively high theoretical capacities. However, in general, their volume changes (>150%) during charge and discharge process have a significant impact, which affects their electrochemical performances. In this paper, nano-alloy FeSb wrapped in three-dimensional honeycomb graphite carbon (FeSb@C) was prepared by the freeze-drying method using sodium chloride as a template. The three-dimensional carbon can buffer the volume change in the reaction process, increasing the contact area between the electrode and electrolyte. Furthermore, the addition of metallic iron also increases the overall specific capacity and improves its electrochemical performance. As the anode of a lithium-ion battery, the optimized FeSb@C shows excellent electrochemical performance with a specific capacity of 193.0 mAh g^{-1} at a high current density of 5 A g^{-1} , and a reversible capacity of 607.8 mAh g^{-1} after 600 cycles of 1 A g^{-1} . It provides an effective strategy for preparing high-performance lithium-ion batteries anode materials.

Keywords: lithium-ion battery; anode; FeSb; carbon coating



Academic Editor: Torsten Brezesinski

Received: 27 June 2025

Revised: 31 July 2025

Accepted: 7 August 2025

Published: 8 August 2025

Citation: Jia, N.; Nie, X.; Li, J.; Qin, W. Nano-Alloy FeSb Wrapped in Three-Dimensional Honeycomb Carbon for High-Performance Lithium-Ion Batteries. *Batteries* **2025**, *11*, 305. <https://doi.org/10.3390/batteries11080305>

Copyright: © 2025 by the authors. Licensee MDPI, Basel, Switzerland. This article is an open access article distributed under the terms and conditions of the Creative Commons Attribution (CC BY) license (<https://creativecommons.org/licenses/by/4.0/>).

1. Introduction

Lithium-ion batteries (LIBs) are considered as promising green energy storage devices because of their high energy density, long cycle life and no memory effect [1–3]. Compared with traditional nickel-chromium batteries, nickel-hydrogen batteries and lead-acid batteries, the energy densities of LIBs are about 2~3 times higher and the power density is 5~6 times higher [3]. Currently, LIBs are widely used in some portable electronic devices, such as mobile phones, digital cameras, notebook computers and electric vehicles [4]. However, with the development of society, people have higher requirements for the safety, efficiency and energy density of commercial LIBs. LIBs are mainly composed of five parts: anode material, cathode material, electrolyte, separator and casing, among which the electrode material plays a vital role in the performance [5,6]. However, graphite, as the traditional commercial negative electrode material of LIBs, is limited by its theoretical lithium storage capacity (372 mAh g^{-1}) [7–11]. Therefore, it is important to find electrode materials with a low cost and high specific capacity [12].

Metal antimony is a promising anode material for rechargeable batteries due to its high theoretical capacity, abundant resources and excellent two-dimensional folded layered structure. However, pure antimony will undergo serious volume changes during charging

and discharging, which will lead to structural collapse and particle crushing, and then affect its stability [13–15]. Various strategies can be used to improve the stability of Sb anode materials. An effective strategy is to reduce the size of Sb into one-dimensional, two-dimensional or three-dimensional space and compound it with carbon material. For instance, Yu et al. prepared a kind of Sb@C nanosphere anode material with an egg yolk-shell structure by a nano-confinement current displacement method [16]. As the anode of LIBs, it exhibits a large specific capacity (634 mAh g^{-1}) and good cycle stability with a specific capacity of 405 mAh g^{-1} at a current density of 1000 mA g^{-1} after 300 cycles. In this way, the internal void space of the hollow yolk shell ball allows the Sb nanoparticles to fully expand during the charging and discharging process, maintaining the structural integrity of Sb@C and the stable SEI film, thus showing excellent performance. However, the composite material formed by Sb and carbon will reduce the overall capacity and stability because of the carbon content. Consequently, different metal can be introduced to form an alloy with Sb, and the electrochemical performances of lithium ion storage of the composite material can be further improved [17]. Currently, various different metals are introduced, such Bi, Sn, Cu and Fe. Among those metals, Bi and Sn are also typical anodes of LIBs and they can form alloys with Sb with any composition ratios; thus, the lithium-ion storage performances can be tuned by altering the experimental conditions [18,19]. In addition, some inactive intermetallic compounds such as Cu and Fe have also been investigated as their lithiated products are closely related to their structures, which generally exhibit relatively small volume changes during the charge/discharge process [20]. In those intermetallic compounds, the Sb acts as electrochemical active material for lithium-ion storage while Fe acts as an electronically conducting matrix. Li et al. designed porous nitrogen-doped carbon-coated FeSb composites with three-dimensional structures by using a green salt template method [21]. As the anode of a potassium ion battery, it showed excellent electrochemical performance and pseudo-capacitance performance, delivering a specific capacity of 245 mAh g^{-1} after 1000 cycles at a current density of 3080 mA g^{-1} . The enhanced electrochemical performances were attributed to the increased active sites, improved electric conductivity and enhanced pseudo-capacitance contribution. The FeSb alloy has also been investigated as an anode of LIBs [22]. However, its electrochemical performances are poor due to its relatively low specific capacity and poor cycling stability, which are largely determined by the microstructures.

In this paper, nano-alloy FeSb wrapped in three-dimensional honeycomb graphite carbon was prepared by the freeze-drying method with sodium chloride as a green template for LIBs. The effects of different atmospheres and carbonization temperature on the electrochemical properties of the alloy were investigated. The FeSb particles are uniformly distributed in three-dimensional graphite, and both Fe and Sb participate in the reaction as active materials during charging and discharging, thus improving the specific capacity of the whole material. And the volume expansion of active materials during Li insertion/extraction can be effectively alleviated between alloys. The existence of three-dimensional carbon can also effectively inhibit the volume expansion, shorten the transmission path of lithium ions in electrode materials, improve the conductivity of materials, increase the specific surface area, and provide more active sites for the reaction.

2. Experimental Section

2.1. Material Synthesis

The citric acid (used as carbon source, analytical reagent, Damao Chemical Reagent Partnership Enterprise, Tianjin, China), sodium chloride (used as template, analytical reagent, Sinopharm Chemical Reagent Co., Ltd., Shanghai, China), antimony potassium tartrate ($\text{C}_8\text{H}_4\text{K}_2\text{O}_{12}\text{Sb}_2$, analytical reagent, Maya Reagent Co. Ltd., Jiaxing, China) and iron

acetylacetone ($C_{15}H_{21}FeO_6$, analytical reagent, Meryer Chemical Technology Co., Ltd., Shanghai, China) were bought and used directly without further purification. The specific synthesis process of FeSb@C is as follows: firstly, 2.0 g citric acid and 10.0 g sodium chloride were dissolved in 50 mL deionized water. After that, 0.6688 g $C_8H_4K_2O_{12}Sb_2$ and 0.706 g $C_{15}H_{21}FeO_6$ were added into the solution and stirred until they are completely dissolved. The precursor was collected via centrifuging with deionized water, freeze-drying [23–25] and treated at temperatures of 600, 700 and 800 °C for 2 h in argon/hydrogen (5%). After the treatment, the NaCl template was removed by washing with DI water for 3 times and the final products were obtained after drying in a vacuum oven at 100 °C for 10 h, which were denoted as FeSb@C-Ar/H₂-6, FeSb@C-Ar/H₂-7 and FeSb@C-Ar/H₂-8, respectively.

2.2. Material Characterization

X-ray diffraction (XRD, Bruker D8, Karlsruhe, Germany) used to characterize the structure was performed with Cu K α radiation ($\lambda = 0.1542$ nm, $V = 40$ kV, $I = 40$ mA) at a scanning rate of $0.05^\circ s^{-1}$ in the range of 15 – 80° . A scanning electron microscope (SEM, JSM-6510, JEOL, Tokyo, Japan), transmission electron microscope (TEM, JEOL JEM 2100F, JEOL, Tokyo, Japan), energy dispersive spectroscopy (EDS) and X-ray photoelectron spectroscopy (XPS, Thermo ESCALAB 250XI XPS, Thermo Scientific, Waltham, MA, USA) equipped with an energy dispersive spectrometer are used to observe the morphology and valence state of chemical elements. The Brunauer–Emmett–Teller (BET, Autosorb-IQ, Anton Paar QuantaTec Inc., Boynton Beach FL, USA) surface area analysis was used to study the pore size distribution and specific surface area. Thermogravimetric analysis (TGA) was performed using a TA instrument (Q500, TA Instruments, New Castle, DE, USA) in air at a temperate range from room temperature to 800 °C with a heating rate of $10\text{ }^\circ\text{C min}^{-1}$.

2.3. Electrochemical Characterization

The electrochemical performances of the as-prepared samples were evaluated by assembling CR2032 coin-type half cells. The working electrode was prepared by mixing the active material, acetylene black powder (conducting agent), and polyvinylidene fluoride (PVDF) with a weight ratio of 7:2:1 in N-methylpyrrolidone solvent. The resulting slurry was coated on copper foil followed by drying in a vacuum dryer at 80 °C for 8 h. Subsequently, the coated copper was cut into small round tablets (8 mm in diameter) as the electrode of LIBs. CR2032 coin-type cells were assembled in an argon-filled glove box, of which the working electrode, separator, counter and reference electrode were made of active materials, Celgard 3501 and lithium foil. The electrolyte was 1 M LiPF₆ dissolved in EC:DEC:EMC with a volume ratio of 1:1:1. The galvanostatic charge–discharge and rate performance were tested on the Neware instrument in the voltage range of 0.01–2.8 V. The cyclic voltammetric (CV) measurements were conducted on the electrochemical workstation (760E) at a scan rate of 0.1 mVs^{-1} from 0.01 to 2.8 V. Electrochemical impedance spectroscopy (EIS) was collected in a frequency range 10^{-1} – 10^6 Hz, and the maximum working AC voltage was set to 5 mV.

3. Results and Discussion

Figure 1a shows the XRD patterns of FeSb@C-Ar/H₂-6, FeSb@C-Ar/H₂-7 and FeSb@C-Ar/H₂-8. The main diffraction peaks of all the samples are located at 30.7, 43.5, 44.3, 55.0 and 59.9, which correspond to (101), (102), (110), (201) and (103) of the hexagonal phase FeSb (PDF#34-1053), respectively [21]. However, it is noteworthy that the intensities of diffraction peaks of the three samples are different, which is related to the crystallinity of the materials. Thus, it shows that different carbonization temperatures can lead to differences in crystallinity of the prepared samples. Figure 1b–d show the SEM images of

FeSb@C-Ar/H₂-6, FeSb@C-Ar/H₂-7 and FeSb@C-Ar/H₂-8, respectively. As can be seen from Figure 1b–d, three-dimensional honeycomb-like carbon structures are evident in all samples. The carbon skeleton structure can not only effectively regulate the density of FeSb nanoparticles and provide enough space to accommodate the electrolyte, but also effectively prevent the aggregation of FeSb nanoparticles after multiple lithium-ion insertion/extraction reactions and alleviate the volume expansion of the samples during the reaction to some extent, which is beneficial in maintaining good lithium-ion storage performances. In addition, as can be seen in Figure 1b–d, the average size of the FeSb nanoparticles in FeSb @C-Ar/H₂-7 and FeSb@C-Ar/H₂-8 is the smaller than the average size of the FeSb nanoparticles in FeSb@C-Ar/H₂-6. The smaller nanoalloy particles help to shorten the lithium-ion diffusion path when used as an anode of LIBs. Figure 1e,f show the TEM and HRTEM images of FeSb@C-Ar/H₂-7. It can be seen from Figure 1f that the small FeSb nanoparticles are coated with carbon, and the size of FeSb nanoparticles is ca. 20–40 nm. It is believed that the sodium chloride template is key to the formation of this carbon structure [26,27]. From the HRTEM, one can clearly observe the lattice of FeSb where the lattice spacing is 0.290 nm, which corresponds to the (101) crystal plane of FeSb (PDF#34-1053) [28,29]. Figure 1g schematically shows the synthesis procedure of the samples. Initially, the precursors are attached to the surface of the NaCl template and after freeze-drying, thermal treatment and removing the NaCl template, the samples were finally obtained.

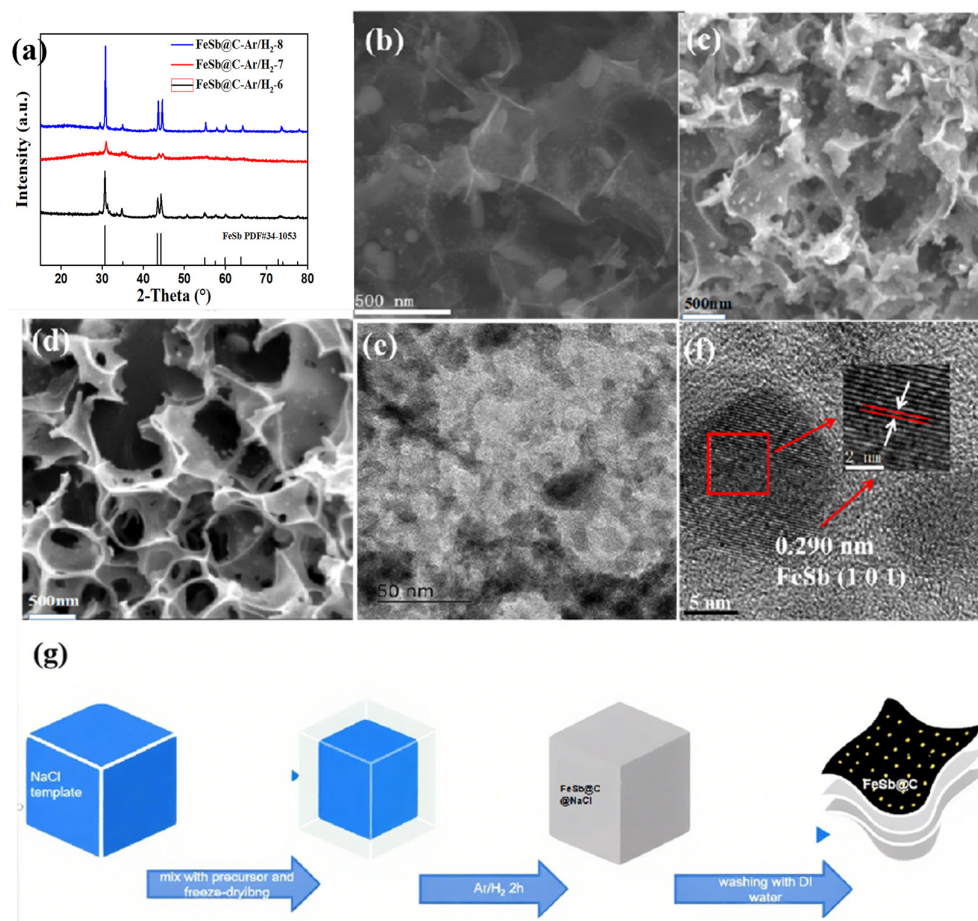


Figure 1. (a) XRD patterns of FeSb@C-Ar/H₂-6, FeSb@C-Ar/H₂-7 and FeSb@C-Ar/H₂-8; SEM images of (b) FeSb@C-Ar/H₂-6, (c) FeSb@C-Ar/H₂ and (d) FeSb@C-Ar/H₂-8; (e) TEM and (f) HRTEM images of FeSb@C-Ar/H₂-7; (g) schematics depicting the fabrication procedure.

The XPS spectra of FeSb@C-Ar/H₂-7 are recorded and shown in Figure 2 to analyze their chemical states. Figure 2a shows the survey scan spectrum and it can be seen that there are Fe, Sb, C and O elements in the sample. From Figure 2b, it is evident that the C1s of the sample can be fitted into four peaks, among which the main peak of the sp² hybrid graphite C atom is located at 284.8 eV. The other three peaks located at 286, 288.9 eV and 290.0 eV correspond to C-O-C, C = O and O-C = O, respectively [30]. Figure 2c shows the spectrum of Fe2p, where the peaks at 711.5 and 713.2 eV are 2p_{3/2} of Fe (III) and Fe (II) and the peaks at 729.8 eV and 725.6 eV are 2p_{1/2} of Fe (II) ion and Fe (III) ion, respectively. In addition, the peaks located at 715.7 eV and 733.5 eV correspond to the satellite peaks of Fe(II) ions [31–33]. In the Sb spectrum of Figure 2d, the peaks at 531.0 eV and 540.6 eV are attributed to 3d_{3/2} and 3d_{5/2} of Sb(III) [21,34–36]. Furthermore, it can be seen that the sample may contain some Sb₂O₃, and the possible reasons are as follows: citric acid is used as a carbon source in the precursor, and oxygen-containing functional groups are contained in the pyrolysis process, which oxidizes Sb²⁺ and then forms Sb₂O₃ [37]. Furthermore, one can observe that the O exists in two states, namely lattice oxygen and adsorbed oxygen, in which the adsorbed oxygen can introduce oxygen vacancies, thus promoting the conversion of electrons [21].

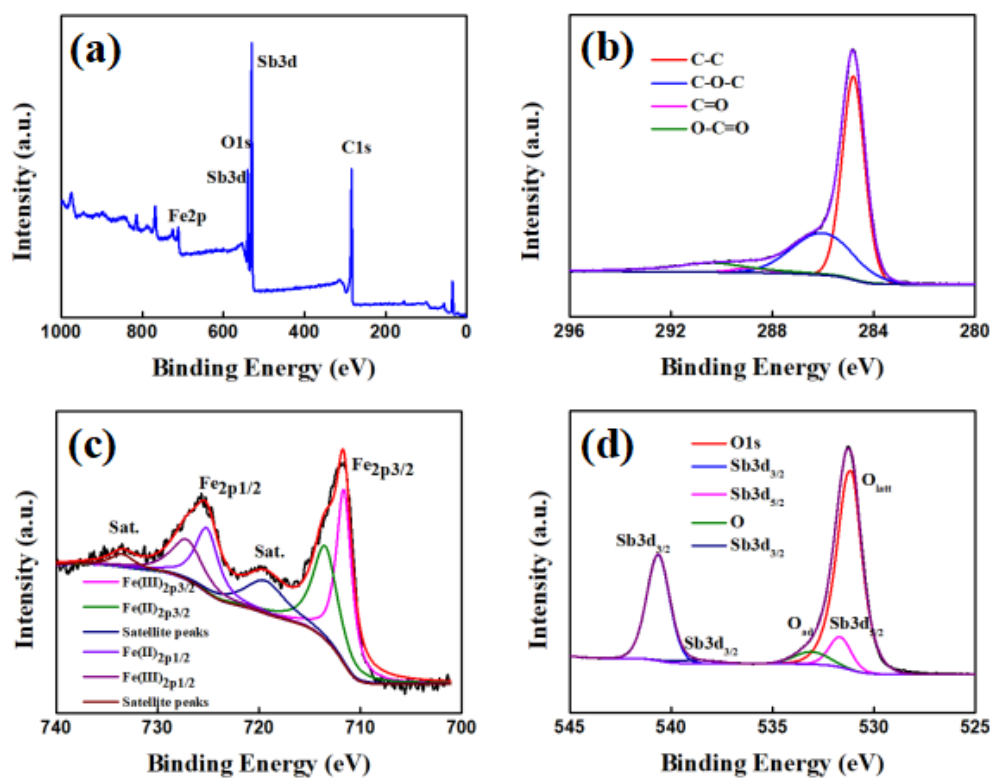


Figure 2. XPS spectra: (a) survey scan and high-resolution spectra of (b) C1s, (c) Fe2p and (d) Sb3d of FeSb@C-Ar/H₂-7.

Figure 3a,b show the adsorption/desorption isotherms and pore size distribution of FeSb@C-Ar/H₂-6, FeSb@C-Ar/H₂-7 and FeSb@C-Ar/H₂-8. All the samples exhibit type II isotherm characteristics with H1 hysteresis loops [38]. The specific surface areas of the samples are 272.4, 495.6 and 366.2 m²g⁻¹, among which FeSb@C-Ar/H₂-7 has the largest specific surface area. The larger specific surface area can increase the contact between anode materials and electrolyte, which is beneficial in the penetration of the electrolyte and provides more channels for the transmission of lithium ions [39,40]. We summarized the specific surface area and total pore volume of all the samples and the results are shown in Table 1. In addition, from the pore size distributions of these samples, one can see that all

the samples are mainly composed of micropore and mesopores with pore sizes in the range of 1–20 nm [41]. The mesopores (2–50 nm) can increase the active sites, and the micropores (<2 nm) enable lithium ions to enter the interior of three-dimensional carbon, which further hinders the entry of solvents, thus avoiding the decomposition of electrolytes and the formation of excessive SEI films and finally improving the electrochemical performances.

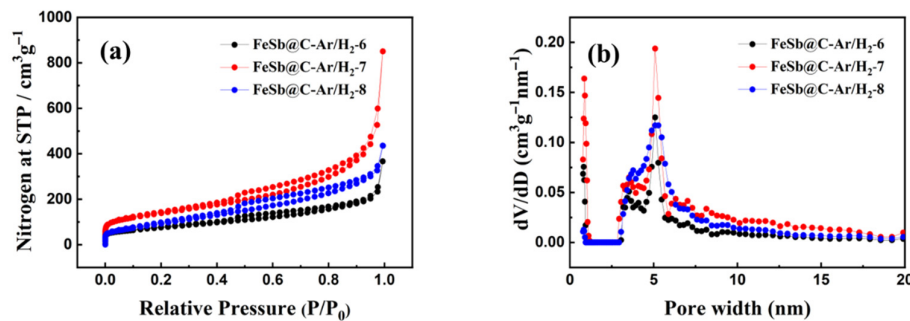


Figure 3. (a) Adsorption–desorption isotherms of N_2 and (b) pore size distribution of $\text{FeSb}@\text{C-Ar}/\text{H}_2\text{-}6$, $\text{FeSb}@\text{C-Ar}/\text{H}_2\text{-}7$ and $\text{FeSb}@\text{C-Ar}/\text{H}_2\text{-}8$.

Table 1. The specific surface area and total pore volume of the as-synthesized samples.

	FeSb@C-Ar/H ₂ -6	FeSb@C-Ar/H ₂ -7	FeSb@C-Ar/H ₂ -8
Specific surface area/m ² /g	272.4	495.6	366.2
Total pore volume/cm ³ /g	0.367	0.851	0.506

To analyze the lithium ions storage mechanism, the CV curve of $\text{FeSb}@\text{C-Ar}/\text{H}_2\text{-}7$ was recorded and is shown in Figure 4a. The reduction peaks that appeared at 0.54, 1.19 and 1.66 V in the first cycle of $\text{FeSb}@\text{C-Ar}/\text{H}_2\text{-}7$ can be attributed to the lithiation of antimony, lithiation and reduction of iron, formation of SEI film and some irreversible reactions [42,43]. In the following cycles, the CV curves highly overlap, which demonstrates that the SEI film formed in the first cycle is relatively stable. In addition, the two reduction peaks that appeared at 0.64 and 1.48 V can be attributed to the lithiation of Sb [44,45] and reduction of Fe^{3+} to Fe^0 [46–49]. The oxidation peaks that appeared at about 1.05 and 1.41 V correspond to the lithium extraction reaction of Li_xSb and the oxidation reaction of Fe, respectively. From the above analysis, it is evident that the reaction process can be described by the following equations:

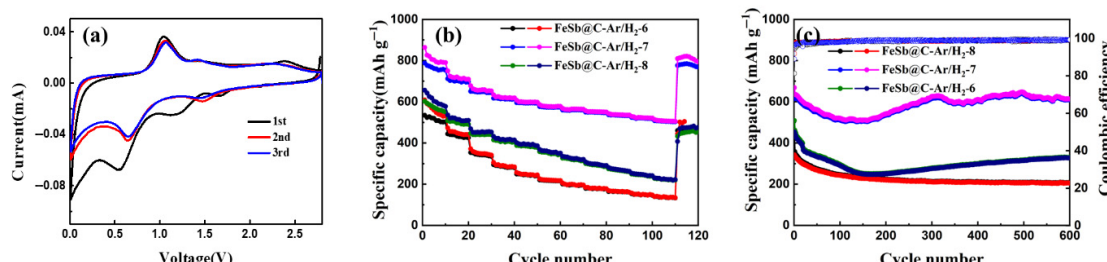
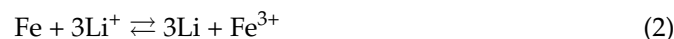


Figure 4. (a) CV curves of $\text{FeSb}@\text{C-Ar}/\text{H}_2\text{-}7$; (b) the rate performance and (c) long cycle performance of $\text{FeSb}@\text{C-Ar}/\text{H}_2\text{-}6$; $\text{FeSb}@\text{C-Ar}/\text{H}_2\text{-}7$ and $\text{FeSb}@\text{C-Ar}/\text{H}_2\text{-}8$ at a current density of 1 A g^{-1} .

The electrochemical performances of these samples were further evaluated by the galvanostatic charge/discharge test. Figure 4b shows the rate performances of FeSb@C-Ar/H₂-6, FeSb@C-Ar/H₂-7 and FeSb@C-Ar/H₂-8, from which one can observe that FeSb@C-Ar/H₂-7 exhibits the best electrochemical performances with reversible capacities of 753.6, 695.5, 644.1, 611.8, 593.5, 573.5, 560.1, 546.6, 532.5, 517.6 and 503.1 mAh g⁻¹ at the current densities of 0.1, 0.2, 0.4, 0.6, 0.8, 1, 1.2, 1.4, 1.6, 1.8 and 2 A g⁻¹. When the current density returned to 0.1 A g⁻¹, the specific capacity also returned to 767.7 for FeSb@C-Ar/H₂-7. In addition, from Figure 4c, one can see that the initial discharge/charge-specific capacities of FeSb@C-Ar/H₂-6, FeSb@C-Ar/H₂-7 and FeSb@C-Ar/H₂-8 are 420.6/341.9, 668.5/613.9 and 509.2/453.3 mAh g⁻¹, corresponding to the coulombic efficiencies of 81.3%, 91.8% and 89.0% at the current density of 1 A g⁻¹. The capacity loss during the first discharge/charge cycle can be attributed to the SEI formation, which agrees with the CV curve of Figure 4a. Furthermore, FeSb@C-Ar/H₂-7 also exhibits the best electrochemical performance with a specific capacity of 607.8 after 600 cycles at a high current density of 1 A g⁻¹. Finally, we have also compared our results with Sb-based anodes for LIBs found in Table 2 and one can see that our results outperform most of those results.

Table 2. Comparison of the electrochemical performances of the FeSb@C composites with those previously reported Sb-based composites.

Samples	Specific Capacity/mAh g ⁻¹	Current Density/mA g ⁻¹	Cycle Numbers	References
Sb@PC	280	1000	500	[13]
Sb@NCFs	480	400	300	[14]
Sb@C	405	1000	300	[16]
Bi0.5Sb0.5@carbon	489.4	1000	2000	[19]
FeSb@C-Ar/H ₂ -7	607.8	1000	600	This work

In order to explore the charge transfer kinetics, the electrochemical impedance spectra of FeSb@C-Ar/H₂-6, FeSb@C-Ar/H₂-7 and FeSb@C-Ar/H₂-8 were measured and the Nyquist plots are shown in Figure 5a. As shown, all the electrochemical impedance spectra are composed of a semicircle in the high frequency region and an inclined line in the low frequency region, in which the concave semicircle can be attributed to the charge transfer resistance (R_{ct}) and the inclined line is attributed to the Warburg impedance (Z_W) related to Li⁺ diffusion [50–53]. In Figure 5a, it is evident that FeSb@C-Ar/H₂-7 has the smallest R_{ct} value among FeSb@C-Ar/H₂-6, FeSb@C-Ar/H₂-7 and FeSb@C-Ar/H₂-8, demonstrating that FeSb@C-Ar/H₂-7 exhibits the best conductivity and the result is in accordance with the electrochemical lithium ion storage performance [54–56].

The CV curves of FeSb@C-Ar/H₂-7 were recorded at different scanning rates to investigate the electrochemical reaction kinetics and the result is shown in Figure 5b. As seen, the shape of CV curve does not change with the change in scanning rate, indicating that the battery has good reversibility. Generally, the relationship between the different peak currents and scanning rates follows the formula presented below [57,58]:

$$\log i = b \log v + \log a$$

where a and b are constants. When b is close to 0.5, the material shows a diffusion control process (refers to the Faraday process, which is related with the insertion and extraction reaction, mainly lithium ion insertion/extraction); when b is close to 1, the battery shows a pseudo-capacitance control process (refers to capacitive process, which is related to highly reversible chemical adsorption, desorption or oxidation, reduction reaction) [59,60]. The calculated b value for FeSb@C-Ar/H₂-7 is 0.72, which is between 0.5 and 1, demonstrating the combination of the diffusion control process and pseudo-capacitance control process.

The detailed contribution of pseudo capacitance can also be calculated according to the following formula [58].

$$i(v) = k_1 v + k_2 v^{1/2}$$

where k_1 and k_2 are constants and $k_1 v$ and $k_2 v^{1/2}$ represent the contribution of pseudo-capacitance behavior and diffusion process, respectively. As shown in Figure 5d, when the scanning rate is 0.1, 0.2, 0.5, 0.8 and 1 mV s⁻¹, the contribution of pseudo-capacitance is 61%, 68%, 78%, 82% and 83%. Pseudo-capacitance behavior can be generated not only on the electrode surface, but also inside the whole electrode, which has faster kinetics than diffusion reaction. Therefore, the remarkable pseudo-capacitance behavior during charging and discharging effectively explains the high-rate performance of FeSb@C-Ar/H₂-7.

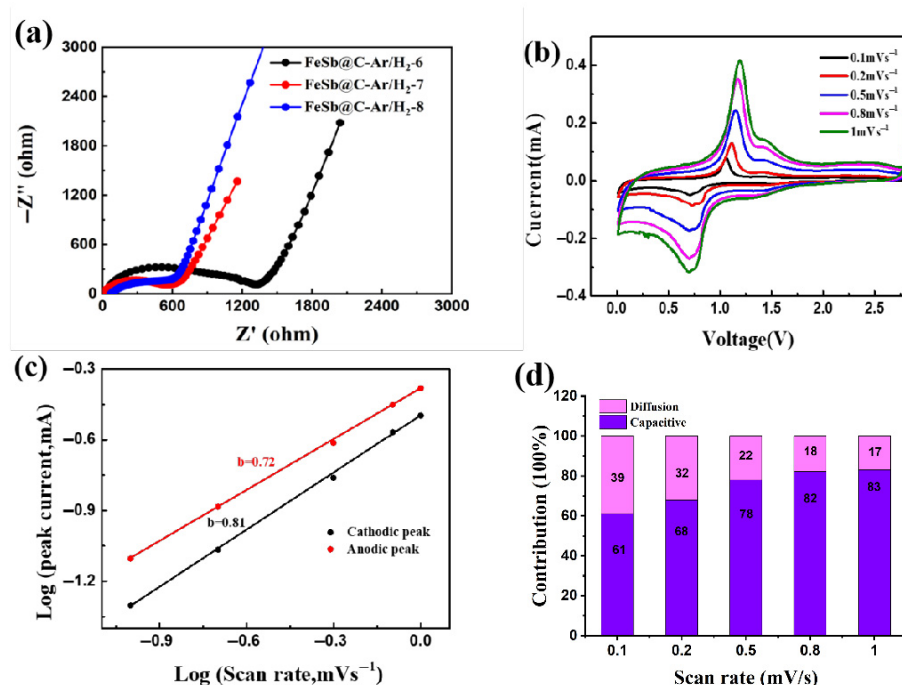


Figure 5. (a) Nyquist plots of FeSb@C-Ar/H₂-6, FeSb@C-Ar/H₂-7 and FeSb@C-Ar/H₂-8; (b) CV curves at different scan rates of FeSb@C-Ar/H₂-7; (c) b value determined with the relationship between peak current and scan rate of FeSb@C-Ar/H₂-7; (d) contribution of capacitive behavior of FeSb@C-Ar/H₂-7 at different scan rates.

4. Conclusions

In summary, FeSb alloy wrapped in three-dimensional honeycomb carbon was prepared by a sodium chloride template-assisted freeze-drying method and applied as anode material of lithium-ion batteries. It was found that FeSb@C-Ar/H₂-7, which was carbonized at 700 °C for 2 h in argon and hydrogen, had an excellent rate performance and long-cycle stability. It delivered a high specific capacity of 193.0 mAh g⁻¹ at a current density of 5 A g⁻¹ and 607.8 mAh g⁻¹ after 600 cycles at a current density of 1 A g⁻¹. These excellent performances were mainly due to the synergistic effect between FeSb alloys and the existence of three-dimensional carbon. The synergistic effect between FeSb alloys not only improved the specific capacity of the whole sample, but also alleviated the volume change during charge/discharge process. The existence of three-dimensional carbon prepared by the freeze-drying method can alleviate the volume expansion and shorten the transmission path of lithium ions, improve the conductivity of the material, increase the specific surface area and provide more active sites for the reaction, thus contributing to the excellent lithium-ion storage performances. In our current work, the effect of the

atomic ratio between Sb and Fe on the electrochemical lithium-ion storage performance was not discussed. More work can be performed to further improve the electrochemical performances. In addition, the initial coulombic efficiency also needs improvement to meet the requirement of practical applications.

Author Contributions: Conceptualization, J.L.; Methodology, N.J. and X.N.; Validation, X.N. and W.Q.; Formal analysis, J.L. and W.Q.; Investigation, N.J.; Resources, J.L.; Writing—original draft, N.J.; Writing—review & editing, X.N., J.L. and W.Q.; Supervision, J.L.; Project administration, J.L. All authors have read and agreed to the published version of the manuscript.

Funding: Financial support was provided by the Natural Science Foundation of Hunan Province (Grant No. 2023JJ30034) and Scientific Research Fund of Hunan Provincial Education Department (Grand No. 23B0295) are acknowledged.

Data Availability Statement: The original contributions presented in this study are included in the article. Further inquiries can be directed to the corresponding author.

Conflicts of Interest: The authors declare no conflict of interest.

References

- Bruce Dunn, H.K.; Tarascon, J.-M. Electrical Energy Storage for the Grid: A Battery of Choices. *Science* **2011**, *334*, 928–935. [[CrossRef](#)]
- Nitta, N.; Wu, F.; Lee, J.T.; Yushin, G. Li-ion battery materials: Present and future. *Mater. Today* **2015**, *18*, 252–264. [[CrossRef](#)]
- Ramasubramanian, B.; Ling, J.; Jose, R.; Ramakrishna, S. Ten major challenges for sustainable lithium-ion batteries. *Cell Rep. Phys. Sci.* **2024**, *5*, 102032. [[CrossRef](#)]
- Kaygusuz, K. Energy for sustainable development: A case of developing countries. *Renew. Sustain. Energy Rev.* **2012**, *16*, 1116–1126. [[CrossRef](#)]
- Wagner, R.; Preschitschek, N.; Passerini, S.; Leker, J.; Winter, M. Current research trends and prospects among the various materials and designs used in lithium-based batteries. *J. Appl. Electrochem.* **2013**, *43*, 481–496. [[CrossRef](#)]
- Nishi, Y. The Development of Lithium Ion Secondary Batteries. *Chem. Rec.* **2001**, *1*, 406–413. [[CrossRef](#)]
- Chen, X.; Li, X.; Ding, F.; Xu, W.; Xiao, J.; Cao, Y.; Meduri, P.; Liu, J.; Graff, G.L.; Zhang, J.G. Conductive rigid skeleton supported silicon as high-performance Li-ion battery anodes. *Nano Lett.* **2012**, *12*, 4124–4130. [[CrossRef](#)]
- Xu, K. Nonaqueous Liquid Electrolytes for Lithium-Based Rechargeable Batteries. *Chem. Rev.* **2004**, *104*, 4303–4417. [[CrossRef](#)]
- Li, B.; Yang, S.; Li, S.; Wang, B.; Liu, J. From Commercial Sponge Toward 3D Graphene-Silicon Networks for Superior Lithium Storage. *Adv. Energy Mater.* **2015**, *5*, 1500289. [[CrossRef](#)]
- Tarascon, J.M.; Armand, M. Issues and challenges facing rechargeable lithium batteries. *Nat. Vol.* **2001**, *414*, 359–367. [[CrossRef](#)]
- Fong, R.; von Sacken, U.; Dahn, J.R. Studies of Lithium Intercalation into Carbons Using Nonaqueous Electrochemical Cells. *J. Electrochem. Soc.* **2019**, *137*, 2009. [[CrossRef](#)]
- Zhang, W.; Qian, M.; Luo, G.; Feng, X.; Wu, C.; Qin, W. Improved lithium ion storage performance of $\text{Ti}_3\text{C}_2\text{Tx}$ MXene@S composite with carboxymethyl cellulose binder. *J. Colloid Interface Sci.* **2023**, *641*, 15–25. [[CrossRef](#)] [[PubMed](#)]
- Wang, H.; Wu, X.; Qi, X.; Zhao, W.; Ju, Z. Sb nanoparticles encapsulated in 3D porous carbon as anode material for lithium-ion and potassium-ion batteries. *Mater. Res. Bull.* **2018**, *103*, 32–37. [[CrossRef](#)]
- Wang, X.; Jia, N.; Li, J.; Liu, P.; Zhao, X.; Lin, Y.; Sun, C.; Qin, W. Sb Nanoparticles Embedded in the N-Doped Carbon Fibers as Binder-Free Anode for Flexible Li-Ion Batteries. *Nanomaterials* **2022**, *12*, 3093. [[CrossRef](#)]
- Qian, M.; Zhang, W.; Luo, G.; Wu, C.; Qin, W. Air-stabilized pore structure engineering of antimony-based anode by electrospinning for potassium ion batteries. *J. Colloid Interface Sci.* **2023**, *633*, 352–361. [[CrossRef](#)] [[PubMed](#)]
- Liu, J.; Yu, L.; Wu, C.; Wen, Y.; Yin, K.; Chiang, F.K.; Hu, R.; Liu, J.; Sun, L.; Gu, L.; et al. New Nanoconfined Galvanic Replacement Synthesis of Hollow Sb@C Yolk-Shell Spheres Constituting a Stable Anode for High-Rate Li/Na-Ion Batteries. *Nano Lett.* **2017**, *17*, 2034–2042. [[CrossRef](#)]
- Xiong, P.; Wu, J.; Zhou, M.; Xu, Y. Bismuth-Antimony Alloy Nanoparticle@Porous Carbon Nanosheet Composite Anode for High-Performance Potassium-Ion Batteries. *ACS Nano* **2020**, *14*, 1018–1026. [[CrossRef](#)]
- Antitomaso, P.; Fraisse, B.; Stievano, L.; Biscaglia, S.; Aymé-Perrot, D.; Girard, P.; Sougrati, M.T.; Monconduit, L. SnSb electrodes for Li-ion batteries: The electrochemical mechanism and capacity fading origins elucidated by using operando techniques. *J. Mater. Chem. A* **2017**, *5*, 6546–6555. [[CrossRef](#)]
- Wang, Y.; Yu, R.; Luo, T.; Ma, G.; Hu, G.; Lyu, J.; Zhou, L.; Wu, J. Solid Solution of Bi and Sb for Robust Lithium Storage Enabled by Consecutive Alloying Reaction. *Small* **2021**, *17*, 2102915. [[CrossRef](#)]

20. He, J.; Wei, Y.; Zhai, T.; Li, H. Antimony-based materials as promising anodes for rechargeable lithium-ion and sodium-ion batteries. *Mater. Chem. Front.* **2018**, *2*, 437–455. [[CrossRef](#)]
21. Li, Z.; Gan, Q.; Zhang, Y.; Hu, J.; Liu, P.; Xu, C.; Wu, X.; Ge, Y.; Wang, F.; Yao, Q.; et al. FeSb@N-doped carbon quantum dots anchored in 3D porous N-doped carbon with pseudocapacitance effect enabling fast and ultrastable potassium storage. *Nano Res.* **2021**, *15*, 217–224. [[CrossRef](#)]
22. Zheng, W.; Yu, X.; Guo, Z.; Song, G.; Hu, F. Magnetron sputtering deposition of MSb(M=Fe, Ni, Co) thin films as negative electrodes for Li-ion and Na-ion batteries. *Mater. Res. Express* **2019**, *6*, 056410. [[CrossRef](#)]
23. Guo, S.; Bai, Y.; Geng, Z.; Wu, F.; Wu, C. Facile synthesis of $\text{Li}_3\text{V}_2(\text{PO}_4)_3/\text{C}$ cathode material for lithium-ion battery via freeze-drying. *J. Energy Chem.* **2019**, *32*, 159–165. [[CrossRef](#)]
24. Wang, S.; Wang, R.; Zhao, Q.; Ren, L.; Wen, J.; Chang, J.; Fang, X.; Hu, N.; Xu, C. Freeze-drying induced self-assembly approach for scalable constructing MoS₂/graphene hybrid aerogels for lithium-ion batteries. *J. Colloid Interface Sci.* **2019**, *544*, 37–45. [[CrossRef](#)]
25. Jakubowska, E.; Lulek, J. The application of freeze-drying as a production method of drug nanocrystals and solid dispersions—A review. *J. Drug Deliv. Sci. Technol.* **2021**, *62*, 102357. [[CrossRef](#)]
26. Xu, Y.; Li, W.; Zhang, F.; Zhang, X.; Zhang, W.; Lee, C.-S.; Tang, Y. In situ incorporation of FeS nanoparticles/carbon nanosheets composite with an interconnected porous structure as a high-performance anode for lithium ion batteries. *J. Mater. Chem. A* **2016**, *4*, 3697–3703. [[CrossRef](#)]
27. Ren, X.; Ai, D.; Zhan, C.; Lv, R.; Kang, F.; Huang, Z.-H. NaCl-template-assisted freeze-drying synthesis of 3D porous carbon-encapsulated V₂O₃ for lithium-ion battery anode. *Electrochim. Acta* **2019**, *318*, 730–736. [[CrossRef](#)]
28. Allcorn, E.; Manthiram, A. High-rate, high-density FeSb–TiC–C nanocomposite anodes for lithium-ion batteries. *J. Mater. Chem. A* **2015**, *3*, 3891–3900. [[CrossRef](#)]
29. Liang, J.-C.; Zhou, K.-Y.; Chen, G.-Y.; Zhang, W.-X.; Liu, J.-A.; Zhang, W.-Z.; Zhang, Z.-P.; Hou, W.; Zhou, M.; Liu, G.-F.; et al. Embedding FeSb alloy nanoparticles in N-doped carbon layers as an efficient bifunctional electrocatalyst for zinc-air battery. *J. Solid State Electrochem.* **2017**, *21*, 3315–3324. [[CrossRef](#)]
30. Li, C.; Wang, Y.; Li, H.; Liu, J.; Song, J.; Fusaro, L.; Hu, Z.-Y.; Chen, Y.; Li, Y.; Su, B.-L. Weaving 3D highly conductive hierarchically interconnected nanoporous web by threading MOF crystals onto multi walled carbon nanotubes for high performance Li-Se battery. *J. Energy Chem.* **2021**, *59*, 396–404. [[CrossRef](#)]
31. Huang, Y.; Li, Y.; Huang, R.; Ji, J.; Yao, J.; Xiao, S. One-pot hydrothermal synthesis of N-rGO supported Fe₂O₃ nanoparticles as a superior anode material for lithium-ion batteries. *Solid State Ion.* **2021**, *368*, 115693. [[CrossRef](#)]
32. Wang, S.; Zhu, Y.; Sun, X.; Liu, H.; Cui, J.; Zhang, Y.; He, W. N, S co-doped modified graphene/Fe₂O₃ composites synthesized via microwave-assisted method for Na-ion batteries. *Inorg. Chem. Commun.* **2020**, *121*, 108188. [[CrossRef](#)]
33. Wang, J.; Yang, X.; Wang, Y.; Jin, S.; Cai, W.; Liu, B.; Ma, C.; Liu, X.; Qiao, W.; Ling, L. Rational design and synthesis of sandwich-like reduced graphene oxide/Fe₂O₃/N-doped carbon nanosheets as high-performance anode materials for lithium-ion batteries. *Chem. Eng. Sci.* **2021**, *231*, 116271. [[CrossRef](#)]
34. Birchall, T.; Connor, J.A.; Hillier, L.H. High-energy Photoelectron Spectroscopy of some Antimony Compounds. *J. Chem. Soc. Dalton Trans.* **1975**, *20*, 2003–2006. [[CrossRef](#)]
35. Deng, M.; Li, S.; Hong, W.; Jiang, Y.; Xu, W.; Shuai, H.; Zou, G.; Hu, Y.; Hou, H.; Wang, W.; et al. Octahedral Sb₂O₃ as high-performance anode for lithium and sodium storage. *Mater. Chem. Phys.* **2019**, *223*, 46–52. [[CrossRef](#)]
36. Feng, X.; Qian, M.; Guo, Z.; Luo, G.; Wu, C.; Qin, W. Graphene modified Sb₂O₃/porous carbon nanofibers via electrospinning treated in air for potassium-ion batteries with enhanced cycling stability. *Int. J. Hydrogen Energy* **2024**, *83*, 326–334. [[CrossRef](#)]
37. Wang, Z.; Dong, K.; Wang, D.; Luo, S.; Liu, X.; Liu, Y.; Wang, Q.; Zhang, Y.; Hao, A.; He, C.; et al. Constructing N-Doped porous carbon confined FeSb alloy nanocomposite with Fe-N-C coordination as a universal anode for advanced Na/K-ion batteries. *Chem. Eng. J.* **2020**, *384*, 123327. [[CrossRef](#)]
38. Chandrasekaran Nithya, G.T. Morphology oriented CuS nanostructures: Superior K-ion storage by surface enhanced pseudocapacitive effects. *Sustain. Energy Fuels* **2020**, *4*, 3574–3587. [[CrossRef](#)]
39. Zhu, W.; Kierzek, K.; Wang, S.; Li, S.; Holze, R.; Chen, X. Improved performance in lithium ion battery of CNT-Fe₃O₄@graphene induced by three-dimensional structured construction. *Colloids Surf. A Physicochem. Eng. Asp.* **2021**, *612*, 126014. [[CrossRef](#)]
40. Peng, Y.-T.; Lo, C.-T. Effect of Microstructure and Morphology of Electrospun Ultra-Small Carbon Nanofibers on Anode Performances for Lithium Ion Batteries. *J. Electrochem. Soc.* **2015**, *162*, A1085–A1093. [[CrossRef](#)]
41. Zhang, L.; Liu, J.; Wang, W.; Li, D.; Wang, C.; Wang, P.; Zhu, K.; Li, Z. Synthesis of N-doped multi-cavity Sn/C composite and utilization to anode in lithium ion batteries. *Mater. Chem. Phys.* **2021**, *260*, 124199. [[CrossRef](#)]
42. He, H.; Sun, D.; Tang, Y.; Wang, H.; Shao, M. Understanding and improving the initial Coulombic efficiency of high-capacity anode materials for practical sodium ion batteries. *Energy Storage Mater.* **2019**, *23*, 233–251. [[CrossRef](#)]
43. Xiao, J.; Li, Q.; Bi, Y.; Cai, M.; Dunn, B.; Glossmann, T.; Liu, J.; Osaka, T.; Sugiura, R.; Wu, B.; et al. Understanding and applying coulombic efficiency in lithium metal batteries. *Nat. Energy* **2020**, *5*, 561–568. [[CrossRef](#)]

44. Liu, Z.; Yu, X.-Y.; Lou, X.W.; Paik, U. Sb@C coaxial nanotubes as a superior long-life and high-rate anode for sodium ion batteries. *Energy Environ. Sci.* **2016**, *9*, 2314–2318. [[CrossRef](#)]
45. Yang, X.; Ma, J.; Wang, H.; Chai, Y.; Yuan, R. Partially reduced Sb/Sb₂O₃@C spheres with enhanced electrochemical performance for lithium ion storage. *Mater. Chem. Phys.* **2018**, *213*, 208–212. [[CrossRef](#)]
46. Wang, H.-G.; Zhou, Y.; Shen, Y.; Li, Y.; Zuo, Q.; Duan, Q. Fabrication, formation mechanism and the application in lithium-ion battery of porous Fe₂O₃ nanotubes via single-spinneret electrospinning. *Electrochim. Acta* **2015**, *158*, 105–112. [[CrossRef](#)]
47. He, C.; Wu, S.; Zhao, N.; Shi, C.; Liu, E.; Li, J. Carbon-encapsulated Fe₃O₄ nanoparticles as a high-rate lithium ion battery anode material. *ACS Nano* **2013**, *7*, 4459–4469. [[CrossRef](#)]
48. Cao, K.; Jiao, L.; Liu, H.; Liu, Y.; Wang, Y.; Guo, Z.; Yuan, H. 3D Hierarchical Porous α -Fe₂O₃Nanosheets for High-Performance Lithium-Ion Batteries. *Adv. Energy Mater.* **2015**, *5*, 1401421. [[CrossRef](#)]
49. Zhu, Z.; Wang, S.; Du, J.; Jin, Q.; Zhang, T.; Cheng, F.; Chen, J. Ultrasmall Sn nanoparticles embedded in nitrogen-doped porous carbon as high-performance anode for lithium-ion batteries. *Nano Lett.* **2014**, *14*, 153–157. [[CrossRef](#)]
50. Rai, A.K.; Anh, L.T.; Gim, J.; Mathew, V.; Kang, J.; Paul, B.J.; Song, J.; Kim, J. Simple synthesis and particle size effects of TiO₂ nanoparticle anodes for rechargeable lithium ion batteries. *Electrochim. Acta* **2013**, *90*, 112–118. [[CrossRef](#)]
51. Xu, Y.; Zhu, Y.; Liu, Y.; Wang, C. Electrochemical Performance of Porous Carbon/Tin Composite Anodes for Sodium-Ion and Lithium-Ion Batteries. *Adv. Energy Mater.* **2013**, *3*, 128–133. [[CrossRef](#)]
52. Lu, G.; Qiu, S.; Liu, J.; Wang, X.; He, C.; Bai, Y.-J. Enhanced Electrochemical Performance of Zn-Doped Fe₃O₄ with Carbon Coating. *Electrochim. Acta* **2014**, *117*, 230–238. [[CrossRef](#)]
53. Luo, G.; Zhou, N.; Feng, X.; Guo, Z.; Wu, C.; Qin, W. Dual-carbon confined Sb₂Se₃ nanorods for potassium ion batteries anode with improved capacity and cycling stability. *J. Energy Storage* **2024**, *87*, 111520. [[CrossRef](#)]
54. Xiong, S.; Lin, X.; Liu, S.; Weng, S.; Jiang, S.; Jiao, Y.; Xu, Y.; Cheng, J. Metal-organic framework derived α -Fe₂O₃ nano-octahedron with oxygen vacancies for realizing outstanding energy storage performance. *Vacuum* **2020**, *182*, 109692. [[CrossRef](#)]
55. Wu, N.; Zhang, Y.; Guo, Y.; Liu, S.; Liu, H.; Wu, H. Flakelike LiCoO₂ with Exposed {010} Facets As a Stable Cathode Material for Highly Reversible Lithium Storage. *ACS Appl. Mater. Interfaces* **2016**, *8*, 2723–2731. [[CrossRef](#)]
56. Gao, G.; Dang, W.; Wu, H.; Zhang, G.; Feng, C. Synthesis of MnWO₄@C as novel anode material for lithium ion battery. *J. Mater. Sci. Mater. Electron.* **2018**, *29*, 12804–12812. [[CrossRef](#)]
57. Zhao, N.; Qin, J.; Chu, L.; Wang, L.; Xu, D.; Wang, X.; Yang, H.; Zhang, J.; Li, X. Heterogeneous interface of Se@Sb@C boosting potassium storage. *Nano Energy* **2020**, *78*, 105345. [[CrossRef](#)]
58. Zhou, J.; Xu, S.; Kang, Q.; Ni, L.; Chen, N.; Li, X.; Lu, C.; Wang, X.; Peng, L.; Guo, X.; et al. Iron oxide encapsulated in nitrogen-rich carbon enabling high-performance lithium-ion capacitor. *Sci. China Mater.* **2020**, *63*, 2289–2302. [[CrossRef](#)]
59. Huang, C.; Xu, A.; Li, G.; Sun, H.; Wu, S.; Xu, Z.; Yan, Y. Alloyed BiSb Nanoparticles Confined in Tremella-Like Carbon Microspheres for Ultralong-Life Potassium Ion Batteries. *Small* **2021**, *17*, e2100685. [[CrossRef](#)]
60. Wang, C.; Zhao, Y.; Zhai, X.; Ding, C.; Zhao, X.; Li, J.; Jin, H. Graphene boosted pseudocapacitive lithium storage: A case of G-Fe₂O₃. *Electrochim. Acta* **2018**, *282*, 955–963. [[CrossRef](#)]

Disclaimer/Publisher’s Note: The statements, opinions and data contained in all publications are solely those of the individual author(s) and contributor(s) and not of MDPI and/or the editor(s). MDPI and/or the editor(s) disclaim responsibility for any injury to people or property resulting from any ideas, methods, instructions or products referred to in the content.